PHILOSOPHICAL TRANSACTIONS A

royalsocietypublishing.org/journal/rsta

Review

Cite this article: Kaufman JL, Vinckevičiūtė J, Kolli SK, Goiri JG, Van der Ven A. 2019 Understanding intercalation compounds for sodium-ion batteries and beyond. *Phil. Trans. R. Soc. A* **377**: 20190020.
http://dx.doi.org/10.1098/rsta.2019.0020

Accepted: 22 May 2019

One contribution of 13 to a discussion meeting issue 'Energy materials for a low carbon future'.

Subject Areas:
materials science, inorganic chemistry, thermodynamics, energy

Keywords:
intercalation compounds, sodium-ion batteries, beyond Li, dislocations, antiphase boundaries, stacking sequence transitions

Author for correspondence:
Anton Van der Ven
e-mail: avdv@ucsb.edu

Downloaded from https://royalsocietypublishing.org/ on 24 February 2025

Understanding intercalation compounds for sodium-ion batteries and beyond

Jonas L. Kaufman, Julija Vinckevičiūtė, Sanjeev Krishna Kolli, Jon Gabriel Goiri and Anton Van der Ven

Materials Department, University of California, Santa Barbara, CA 93106, USA

JLK, 0000-0002-0814-9462; JV, 0000-0002-9921-9605; SKK, 0000-0002-6360-1693; AVV, 0000-0002-2679-8909

Intercalation compounds are popular candidate electrode materials for sodium-ion batteries and other 'beyond lithium-ion' technologies including potassium- and magnesium-ion batteries. We summarize first-principles efforts to elucidate the behaviour of such compounds in the layered and spinel structures. Trends based on the size and valence of the intercalant and the ionicity of the host are sufficient to explain phase stability and ordering phenomena, which in turn determine the equilibrium voltage profile. For the layered structures, we provide an overarching view of intercalant orderings in prismatic coordination based on antiphase boundaries, which has important consequences for diffusion. We examine details of stacking sequence transitions between different layered structures by calculating stacking fault energies and discussing the nature of dislocations. A better understanding of these transitions will likely aid the development of batteries with improved cyclability.

This article is part of a discussion meeting issue 'Energy materials for a low carbon future'.

1. Introduction

Rechargeable Li-ion batteries have been tremendously successful in industrial and consumer applications, and continue to attract attention from the research community in order to find ways of further improving battery performance [1,2]. Efforts are also being made to move beyond Li-ion for low-cost solutions to large-scale energy storage problems. This includes a

THE ROYAL SOCIETY PUBLISHING

© 2019 The Author(s) Published by the Royal Society. All rights reserved.

Downloaded from https://royalsocietypublishing.org/ on 24 February 2025

renewed interest in Na-ion batteries [3] and other less traditional chemistries for batteries that shuttle K [4] and multivalent cations [5,6]. The success of such technologies hinges on the development of new electrolyte and electrode materials that can withstand the extreme chemical and structural changes that often accompany each charge and discharge cycle of a battery.

Many intercalation compounds, particularly layered ones, have been studied as electrode materials for rechargeable batteries. The canonical layered $LiCoO_2$ [7] and related Ni-Mn-Co (NMC) and Ni-Co-Al (NCA) compounds are used as cathodes in many Li-ion battery applications [2,8]. Layered intercalation compounds are similarly the subject of great interest for Na- and K-ion battery electrodes [4,9], though there is some question as to how they will compete with the current state-of-the-art polyanionic compound $Na_3V_2(PO_4)_2F_3$ for Na-ion battery cathodes [10]. A main obstacle is the prevalence of structural phase transitions involving stacking sequence changes of the layers [11–13], which often lead to mechanical degradation and poor cyclability [10,14]. Many of these materials also exhibit strong cation-vacancy ordering tendencies [11,15,16], which result in large jumps in voltage and sluggish diffusion at particular compositions [17,18]. Turning to other host structures such as spinel may offer benefits of better structural stability and high rate capability [19–22]. Though we will primarily discuss intercalation compounds used as cathode materials, all of these considerations apply to anode materials as well.

In exploring various candidate electrode materials for beyond Li-ion batteries, it is critical to understand their fundamental thermodynamic behaviour. Structural phase stability and ordering phenomena have large impacts on many aspects of battery performance including the voltage profile, diffusion rates and degradation mechanisms. Key thermodynamic properties that may be difficult to access experimentally can be readily probed using first-principles statistical mechanics techniques [23–26], which can also be used to examine non-equilibrium kinetic processes [27–31]. Detailed atomic and mesoscale studies of battery electrode materials based on first-principles techniques may offer more clues as to how to avoid unfavourable phase transitions or alleviate their effects.

Na-ion batteries provide a lens through which to examine some effects not typically seen in the more well-studied Li-ion systems, including, in particular, ordering phenomena and structural phase transitions in the electrode materials. Certain underlying trends observed here may extend to other more novel chemistries, such as K-ion batteries, and help explain observations in those largely unexplored composition spaces. Recent progress on beyond Li-ion battery technology, including Na-ion, has been extensively reviewed [3–5,9,32–40]. In this article, we aim to summarize some insights we have gleaned from computational work into the fundamental behaviour of intercalation compounds, with a focus on ordering and stacking sequence changes in layered systems.

2. Thermodynamics

First-principles thermodynamic studies of battery materials begin with a calculation of free energies of the relevant phases. Free energies at zero temperature can be calculated using quantum mechanical techniques such as density functional theory (DFT) [41], while free energies at finite temperature can be calculated with statistical mechanical techniques that build on the ground state results using effective Hamiltonians [25,42]. Figure 1*a* shows the free energy of the layered Na_yTiS_2 intercalation compound, calculated at 300 K [43]. The envelope of equilibrium free energies over the different phases as determined with the common tangent construction delineates the single- and two-phase regions as a function of composition.

The free energies of the electrode materials also embed information about the voltage of a battery. Indeed, the battery voltage is determined by the difference in chemical potential of the intercalating species A between the two electrodes according to

$$V(y) = -\frac{\mu_A(y) - \mu_A^\circ}{ne}, \tag{2.1}$$

Downloaded from https://royalsocietypublishing.org/ on 24 February 2025

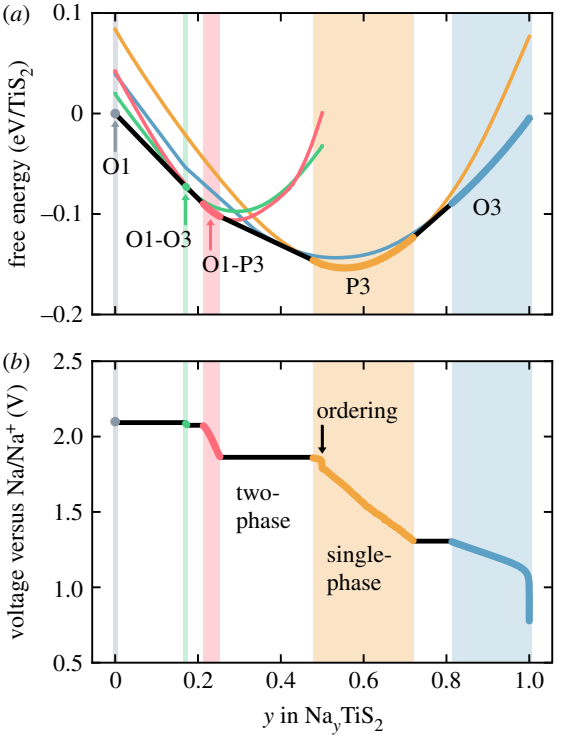

Figure 1. (*a*) Calculated free energy curves of Na_yTiS_2 in different layered host structures at 300 K. The global convex hull of free energies is shown with black lines connecting the curves of each stable phase. (*b*) Voltage curve derived from the free energy at 300 K. Coloured rectangles in the background represent single-phase regions, while black lines correspond to two-phase equilibria. The step at $y = 1/2$ corresponds to a stable ordering of Na ions in P3. (Online version in colour.)

where $\mu_A(y)$ is the chemical potential of A in the cathode at composition y, μ_A° is the chemical potential of A in the reference electrode, n is the number of electrons transferred per A ion and e is the elementary charge. Note that for reversible electrochemical cells, the positive (negative) electrode is technically only defined as the cathode (anode) upon discharge, while the opposite is true upon charge. However, we will continue to use these terms, consistent with much of the literature. With a constant chemical potential in the reference electrode, the voltage is simply related to the chemical potential of the intercalating species in the cathode, which is the slope of free energy versus composition. Through this connection, the meaning of certain features in the voltage profile becomes clear, as illustrated in figure 1*b*. Plateaus correspond to two-phase regions, where the chemical potential is constant, while steps correspond to ordered phases at fixed composition, where the concavity (the energetic strength) of the ordering determines the magnitude of its step. Sloping regions usually correspond to solid solutions. Note that kinetic effects, chemical participation from the electrolyte and other extraneous factors can significantly alter the voltage curve, but the equilibrium voltage curve is an essential starting point for understanding battery performance.

3. Crystallography

We will discuss compounds of the formula $A_yMX_2 (0 \leq y \leq 1)$, where A is an alkali or alkaline earth metal, M is a transition metal and X is oxygen or sulfur. Four key host structures that we will examine are shown in figure 2. The layered (O1, P3, O3) and spinel structures are all based on stacked triangular lattices of X. In the layered compounds (figure 2*a–c*), triangular M layers

Downloaded from https://royalsocietypublishing.org/ on 24 February 2025

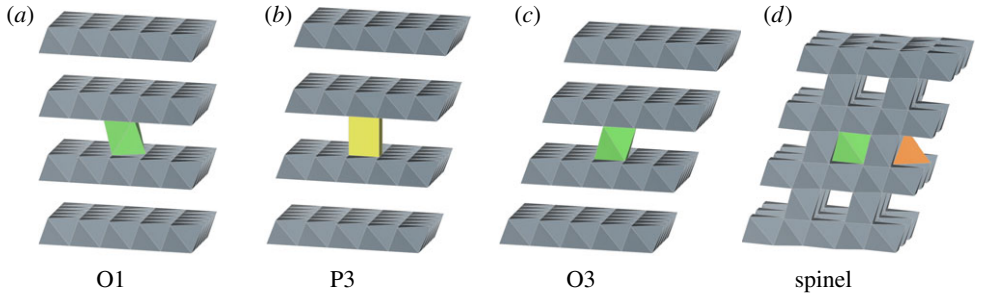

Figure 2. The layered (*a*) O1, (*b*) P3 and (*c*) O3 host structures, in addition to (*d*) the spinel host structure. Grey octahedra represent *M* cations with *X* anions at the corners. Green, yellow and orange are used to show *A* cations in octahedral, trigonal prismatic and tetrahedral coordination, respectively. Structure visualization created using VESTA [44]. (Online version in colour.)

lie between every other pair of *X* layers, forming slabs of edge-sharing MX_6 octahedra separated by van der Waals gaps. The intercalant *A* is inserted into these gaps, and its site topology is determined by the *X* stacking sequence: *A* can occupy octahedral sites in O1 and O3 or trigonal prismatic sites in P3, with the available sites sharing faces with two, one and zero *M* in O1, P3 and O3, respectively. Hybrid structures that switch between different stackings, such as O1–O3, are also seen and are often 'staged,' meaning that the *A* concentration is not the same in every layer [45,46].

Closely related to the layered phases is the spinel structure (figure 2*d*). Spinels are normally represented by the formula AM_2X_4, but with vacancies incorporated on the *A* sites and allowing for octahedral occupancy of the *A* cations, this may also be expressed as A_yMX_2. Spinel shares the face-centred cubic *X* framework of O3, but with one-quarter of the *M* moved from the *M* layers into the gaps. This *M* ordering results in a three-dimensional interconnected network of MX_6 octahedra in which *A* can occupy tetrahedral or octahedral sites, neither of which share faces with *M*.

The commonality of the anion (*X*) sublattices of spinel and O3 make phase transitions between the two kinetically facile. The irreversible transition from O3 to spinel, for example, simply requires the migration of one out of every four *M* from the metal layer to the *A* layers. There is typically a significant driving force for this transition in partially deintercalated Li_yMO_2 (around $y = 1/2$), although it tends to occur quite gradually due to kinetic limitations [8,47]. Such a driving force is notably absent in $Na_{1/2}MO_2$, which has been attributed to the larger size of Na^+ [48]. Note that in the completely deintercalated state ($y = 0$), all layered intercalation compounds tend to be susceptible to decomposition into other phases.

In contrast to the O3-spinel transition, transitions between different layered structures within the O3 family (O3, P3, O1 and their hybrids) are generally reversible and facilitated through the shearing of MX_2 slabs [49]. Though we focus on the O3 family here, there is another family of layered structures based on a distinct set of stackings called the O2/P2 family [50]. Any transition between the two families requires a stacking sequence change of the layers within a single MX_2 slab and is therefore prohibited at room temperature by the energetic cost of breaking *M*–*X* bonds. P2 compounds have received great interest as Na-ion battery electrodes [3,17], but higher capacities are generally achievable with the O3 family because P2 hosts are often not fully intercalated in order to avoid the transition to O2 [51]. O3-type compounds also yield higher voltages since the $NaMX_2$ end member is usually most stable in the O3 structure [52,53].

4. Chemistry

The chemical properties of the intercalant *A* are important in determining its behaviour within an intercalation compound. Consider the intercalants Li, Na, K, Mg and Ca. These exhibit a

Downloaded from https://royalsocietypublishing.org/ on 24 February 2025

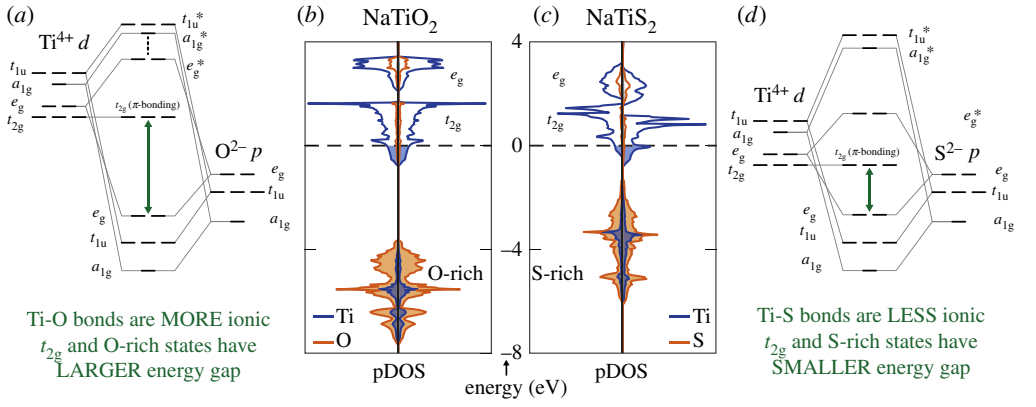

Figure 3. Molecular orbital diagrams for isolated (*a*) TiO_6 and (*d*) TiS_6 octahedra alongside the partial density of states of layered (*b*) $NaTiO_2$ and (*c*) $NaTiS_2$ in the O3 structure. Na density of states is shown in grey, but is negligible in this energy range. (Online version in colour.)

range of ionic radii, with $Mg^{2+} \approx Li^{+} < Ca^{2+} \approx Na^{+} < K^{+}$ (based on the Shannon crystal radii [54] for six-coordination). The ionic radius influences the preferred coordination for each species, as well its migration barriers and the distortions it induces when inserted into a host structure. The difference in valence between monovalent cations (Li^{+}, Na^{+}, K^{+}) and divalent cations (Mg^{2+}, Ca^{2+}) is important not only in setting the battery capacity and voltage but also in scaling the strength of electrostatic interactions within the electrode material. The other key factor for electrostatics is electropositivity, for which Mg < Ca and Li < Na < K. More electropositive species tend to give up more of their electrons, resulting in stronger electrostatic interactions.

The chemistry of the host MX_2 plays a key role in its electronic structure. Electronic structure is often analysed by looking at density of states (DOS) diagrams (or partial DOS (pDOS) where the density is broken up by contributing species), which indicate the density of electrons at specific energy levels. As a simplified model, consider an isolated octahedron of a transition metal such as Ti surrounded by six ligand species (e.g. O or S). The degeneracy of the transition-metal *d* orbitals is split by the ligand field according to the O_h symmetry group in a perfect octahedron [55,56]. The octahedra in real compounds are often distorted such that the degeneracy of the orbitals is reduced further (for example, the octahedral transition-metal environments in the layered structures are typically trigonally compressed along the stacking direction, lowering their symmetry to D_{3d}).

The *d* orbitals of the transition metal and the *p* orbitals of the ligand readily interact to form hybridized states. Molecular orbital diagrams depicting the hybridization between these species are shown in figure 3*a*, *d* for perfect TiO_6 and TiS_6 octahedra, respectively. We have shown only σ-bonding (no π-bonding) in these simplified diagrams. The states within each species' orbitals can be assigned to a symmetry group representation, and only states with the same representation can hybridize. Note, for instance, that there are no available t_{2g} O or S states to σ-bond with the available t_{2g} Ti states (though it turns out they can hybridize via π-bonds). When states hybridize, they split into low-energy bonding and high-energy antibonding (indicated by an asterisk) hybridized states. Electrons fill lowest energy states first (i.e. from the bottom of the diagram up), filling up to around the t_{2g} states for materials discussed in this work. The bonding states (e.g. t_{1u} and a_{1g}) are below the energy of the isolated ligand *p* states, are filled first, and have mainly ligand character; the antibonding states (e_g^*, a_{1g}^* and t_{1u}^*) are above their respective Ti states and therefore have largely transition-metal character.

The available states in TiO_6 are identical to those in TiS_6 and it is only the relative energy of the states that differs between the two chemistries. The more ionic the *M*-ligand pair (i.e. the greater their electronegativity difference), the further apart in energy the hybridized states

Downloaded from https://royalsocietypublishing.org/ on 24 February 2025

will reside, which can be seen in comparing the pDOS of layered $NaTiO_2$ and $NaTiS_2$ crystals (figure 3*b*,*c*). The intercalant (in this case, Na) serves largely as an electron donor and is generally not considered to hybridize with the transition metals or ligands. However, increased intercalant concentration does raise the Fermi level as more electronic states are filled. For instance, Ti^{4+} in TiX_2 has a d^0 electronic configuration while Ti^{3+} in $NaTiX_2$ results in d^1, corresponding to one electron beginning to fill the t_{2g} states.

When an octahedron is in a crystal, the localized states spread out into bands and new, more complicated symmetries are introduced. However, we can approximate the regions in the pDOS diagram as ligand-rich states, t_{2g}-like states, and e_g-like states. The dashed line at the top of the filled states indicates the Fermi level, which is conventionally set to 0 eV. We see that the decrease in ionicity between Ti and S (when compared with O) results in a considerable decrease in the energy gap between the S-rich states and the e_g and t_{2g} states. Since electronic structure plays a role in conductivity, magnetization and even structural changes, understanding the effects of different transition metal and ligand pairings is instrumental in material design. Oxides tend to be more ionic than sulfides due to the high electronegativity of O. The transition metal identity can also have a significant effect. We have focused on the TiS_2 and CoO_2 hosts, as the itinerant nature of their valence electrons and absence of Jahn–Teller activity makes these good model systems for examining fundamental behaviour.

5. Trends in phase stability

A high-throughput study of layered A_yTiS_2 and A_yCoO_2 (A = Li, Na, K, Mg, Ca) identified key trends in phase stability and the energetic factors underlying them [57]. Three important factors are depicted in figure 4 and can be explained in terms of size considerations and varying strengths of competing electrostatic interactions between different cations. The strength of these electrostatic effects depends significantly on the ionicity of the compound [57]. This simplified picture does not include purely steric effects or highly covalent bonding, but nonetheless accounts for much of the observed behaviour.

The relative stability between prismatic and octahedral A coordination is strongly influenced by X–X interactions. Prismatic coordination leads to a shorter interlayer X–X distance than octahedral coordination for fixed A and X ionic radii (figure 4*a*). Smaller intercalants such as Li are therefore unstable in prismatic coordination because the X anions are too close together, while larger intercalants such as Na and K do not penalize the host when it adopts a P3 or P2 structure.

Face-sharing between AX_6 polyhedra and MX_6 octahedra also influences the stability of different layered structures due to the repulsive nature of the short-range A–M interactions (figure 4*b*). In P3, each A site shares a face with one MX_6 octahedron, while in O3 there is no face-sharing. More ionic compounds, therefore, tend to adopt O3 at high compositions to avoid the electrostatic repulsion of face-sharing sites. The octahedral sites of O1 share faces with both neighbouring MX_6 octahedra, making O1 unstable for any intercalant concentration in more ionic compounds. More covalent compounds, however, tend to adopt O1 over the full composition range, which has been ascribed to a diminished repulsion between X p orbitals in the gap between layers [58].

The topology of the A sites within each host plays an important role in determining the type of ordered phases that are possible at intermediate intercalant compositions. In more ionic compounds, repulsive electrostatic interactions will strive to separate the A cations as far apart from each other as possible within each intercalant layer. In P3, the available prismatic A sites form a honeycomb network, which allows for A–A distances that are not available on the triangular lattice of octahedral A sites in O3. This tends to stabilize P3 at intermediate concentrations when the benefit of maximizing A–A distances on the honeycomb network outweighs the penalty for face-sharing. Repulsive interactions on the honeycomb network can lead to intricate A orderings which will be discussed later.

A systematic study of spinel A_yTiS_2 and A_yCoO_2 (A = Li, Na, Mg) revealed similar trends in these compounds [22]. Here the host structure is fixed and intercalants may occupy either

Downloaded from https://royalsocietypublishing.org/ on 24 February 2025

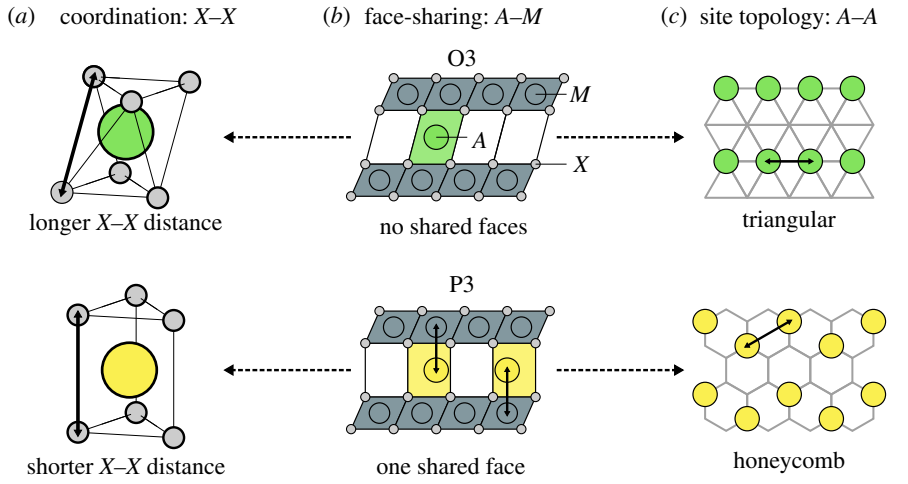

Figure 4. Important electrostatic interactions that determine phase stability in AMX_2 layered intercalation compounds, illustrated using O3 and P3 as examples. (*a*) Interlayer *X*–*X* distances determine whether prismatically coordinated *A* are stable. (*b*) Face-sharing results in energetically unfavourable *A*–*M* interactions (*c*) The sites available to intercalants determine the possible orderings that limit *A*–*A* interactions. (Online version in colour.)

octahedral or tetrahedral sites, the relative stability of which is determined by two competing factors: larger cations favour the octahedral sites because they offer more space, while tetrahedral sites allow *A* cations to lie further away from neighbouring *M* cations and limit *A*–*M* interactions. The latter is more important in more ionic hosts, much like the face-sharing penalty in the layered structures.

In the layered and spinel structures, phase stability is greatly influenced by the identities of both the host and the intercalant. Electrostatic interactions are stronger in more ionic hosts such as CoO_2 compared to more covalent hosts such as TiS_2. Furthermore, intercalation of a more electropositive species, such as Na compared with Li, results in stronger *A*–*A* and *A*–*M* repulsions. Ion size plays a similar role in the layered structures, as larger ions such as Na and K result in larger interlayer spacing and reduced screening from the *X* anions [46]. Divalent intercalant cations such as Mg and Ca tend to create stronger electrostatic interactions than monovalent ones from the same period, as their charge is doubled [59,60].

To examine some of the trends in phase stability more closely, we turn to voltage profiles and phase diagrams obtained from first-principles studies [22,28,43,61]. Figure 5 shows calculated room temperature voltage profiles and phase diagrams of Li_yTiS_2, Na_yTiS_2 and Na_yCoO_2 in the layered (O3-type) and spinel structures. The agreement with available experimental voltage curves, which are shown in red, is quite good. Recall that plateaus correspond to two-phase regions, while steps correspond to ordered phases. The steepness of each curve is related to the strength of *A*–*A* repulsion, which reflects the ionicity of the compound: the Na_yCoO_2 voltage curves in figure 5*c*,*f* are noticeably steeper than their respective Na_yTiS_2 counterparts in figure 5*b*,*e*. The particular characteristics of the transition metal, such as on-site electron repulsion, can also affect the slope and average value of the voltage. For oxides, a systematic underprediction of the voltage is not uncommon when using DFT (without additional corrections such as a Hubbard *U*) [66].

Layered Li_yTiS_2 is quite covalent and remains O1 at all Li concentrations (figure 5*a*). Mg_yTiS_2 (not shown) behaves quite similarly [59]. Na_yTiS_2, conversely, stabilizes O3 at high Na concentrations and P3 at intermediate concentrations (figure 5*b*). O1 is stable only at $y = 0$, while staged hybrid O1–P3 and O1–O3 phases are predicted to be stable at low Na concentrations. Na_yCoO_2 stabilizes similar phases as those adopted by Na_yTiS_2 but there are some important

Downloaded from https://royalsocietypublishing.org/ on 24 February 2025

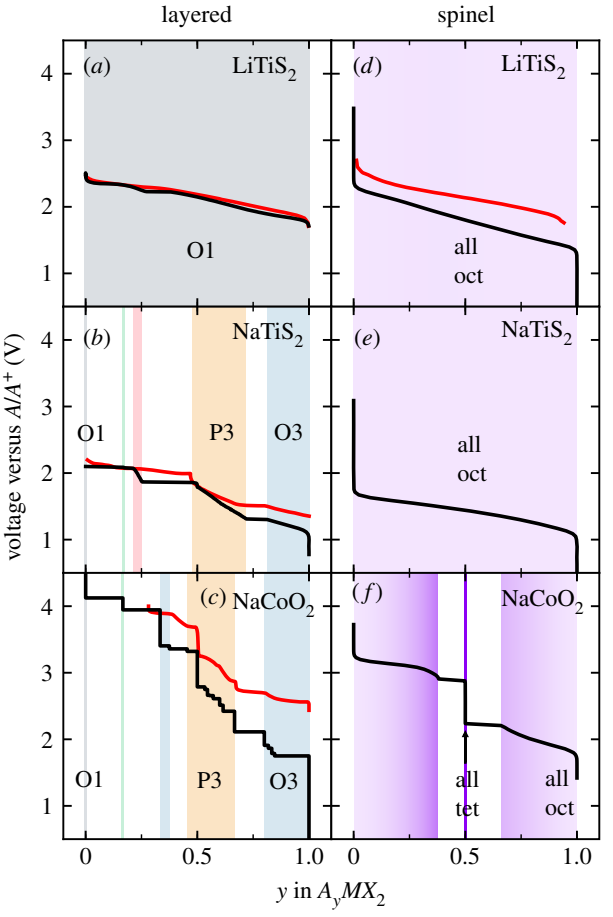

Figure 5. Calculated equilibrium voltage profiles (black) for various layered (*a* [28], *b* [43], *c* [61]) and spinel (*d*,*e*,*f*) [22] intercalation compounds at 300 K. Available experimental curves (red) are shown for comparison in (*a* [62], *b* [63], *c* [64], *d* [65]). Coloured rectangles in the background of (*a*,*b*,*c*) indicate regions in which each layered host structure was found to be stable. Background colour in (*d*,*e*,*f*) indicates the fraction of *A* occupying tetrahedral sites (versus octahedral sites) in the spinel host structure. (Online version in colour.)

differences which reflect the increased ionicity of Na_yCoO_2. The Na_yCoO_2 voltage curve is steeper and contains more steps (the curve shown was actually calculated at zero temperature because none of the ground states were found to disorder at room temperature [61]), with a much larger step at $y = 1/2$ compared to that of $Na_{1/2}TiS_2$ (figure 5*c*). The ordering that produces this step will be discussed in the next section. A significant step near $y = 1/2$ has also been observed in some K intercalation compounds [67,68], which likely corresponds to a similar ordering [69]. P3 is stable up to $y = 2/3$ in Na_yCoO_2 versus $y \approx 0.72$ in Na_yTiS_2, indicating that the face-sharing penalty begins to destabilize P3 sooner in the more ionic Na_yCoO_2. The even more ionic Na_yTiO_2 (not shown) remains O3 throughout cycling [70,71], as face-sharing in P3 is likely even more unfavourable.

In the spinel host, Li_yTiS_2 and Na_yTiS_2 display similar solid solution behaviour resulting in smooth voltage profiles (figure 5*d*,*e*). The intercalants in these compounds occupy only octahedral sites. In the more ionic Na_yCoO_2, tetrahedral and octahedral sites were found to be essentially degenerate, with the energy penalty of the smaller tetrahedral sites being balanced by reduced *A*–*M* interactions [22]. This results in solid solution behaviour with mixed octahedral and tetrahedral occupancy at high and low Na concentrations. However, at $y = 1/2$ the compound orders with

Downloaded from https://royalsocietypublishing.org/ on 24 February 2025

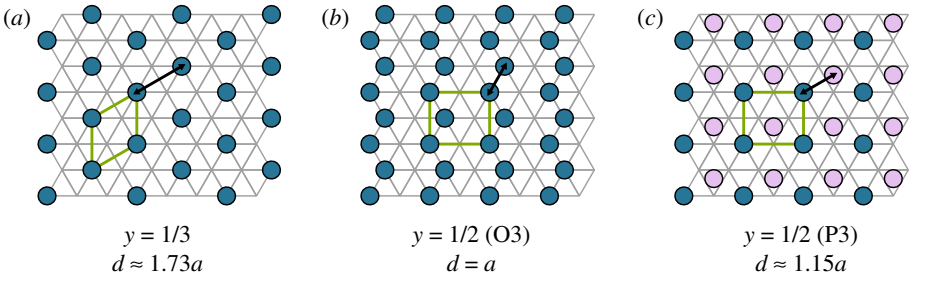

Figure 6. Typical low-energy *A* orderings predicted at (*a*) $y = 1/3$ in O3 and P3, (*b*) $y = 1/2$ in O3 and (*c*) $y = 1/2$ in P3. *a* is the lattice parameter and *d* is the shortest *A*–*A* distance. Dark blue and light purple are used to distinguish between the two different triangular sublattices. (Online version in colour.)

Na filling all the tetrahedral sites, thereby maximizing the distances between Na cations. This ordering produces a significant step in the voltage curve, with two-phase regions on either side (figure 5*f*). Mg, being a divalent cation, produces stronger electrostatic interactions than Na, stabilizing some tetrahedral occupancy in Mg_yTiS_2 and multiple ordered phases in Mg_yCoO_2 (not shown) [22,60].

In the following sections, we focus on ordering and structural changes that can occur in layered intercalation compounds. First, we present the rich intercalant orderings that appear in more ionic compounds and then we discuss the mechanisms for structural phase transitions between layered structures.

6. Intercalant orderings

Larger intercalants such as Na and K tend to form ordered phases in more ionic hosts, which manifest themselves as steps in the voltage profiles. Both the O3 and P3 structures favour the hexagonal ground state ordering at $y = 1/3$, shown in figure 6*a* [43,61,69]. This ordering maximizes the distance between *A* cations where the shortest *A*–*A* distance is $d = \sqrt{3}a \approx 1.73a$ (*a* being the lattice parameter). At $y = 1/2$, however, it is not possible to arrange the *A* ions on a single triangular sublattice without occupying adjacent nearest-neighbour sites with separation $d = a$ (figure 6*b*). Orderings at $y = 1/2$ in O3 are, therefore, frustrated in the sense that they must include this electrostatically unfavourable interaction [57]. However, if a second triangular sublattice is available, as in P3, the *A* ions can spread out slightly further to achieve a separation of $d = 2a/\sqrt{3} \approx 1.15a$. This is realized in the zig-zag row ordering at $y = 1/2$ shown in figure 6*c*, which is observed in many Na intercalation compounds in both the P3 and P2 structures [33,64,72–74].

The honeycomb network of *A* sites in P3 yields many more possible orderings than O3, which can result in very complex ground states at intermediate intercalant concentrations. However, a unifying picture of these orderings is revealed by considering them as regions of one ordering separated by antiphase boundaries (APBs). For example, in Na_yTiS_2, the P3 orderings at room temperature for $y > 1/2$ are predicted to consist of triangular islands of Na occupying a single sublattice, as shown in figure 7*a* [43]. The APBs formed along the edges of the triangular domains introduce vacancies into the structures. The total length of APBs, therefore, determines the composition. Another example is in Na_yCoO_2, where the zig-zag row ordering at $y = 1/2$ is much stronger than in Na_yTiS_2. As such, the orderings immediately above and below $y = 1/2$ preserve this ordering locally, but include APBs to accommodate changes in Na composition. There are two types of boundaries that introduce either more vacancies (diluted) or more Na (enriched), as shown in figure 7*b*,*c* [61]. More complicated orderings are predicted between $y = 4/7$ and $y = 2/3$ that are based on the $y = 4/7$ ground state periodically separated by another type of 'enriched' APB. More details about the precise orderings are reported in [61]. The same intercalant ordering preferences have been predicted for K_yCoO_2 in the P3 structure [69].

Downloaded from https://royalsocietypublishing.org/ on 24 February 2025

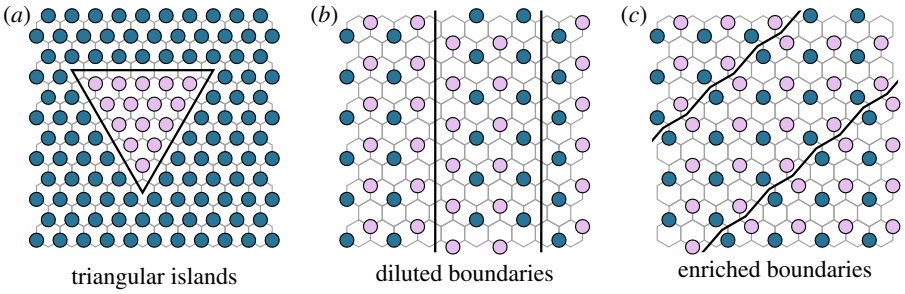

Figure 7. Different types of antiphase boundaries predicted to appear on the honeycomb network in P3. (*a*) Vacancies congregate along boundaries to form triangular island domains at high compositions. At intermediate compositions, two types of boundaries incorporate (*b*) additional vacancies or (*c*) additional *A* ions between regions of the $y = 1/2$ ordering from figure 6*c*. Dark blue and light purple are used to distinguish between the two different triangular sublattices. (Online version in colour.)

In both Na_yTiS_2 and Na_yCoO_2, stable ordered superstructures are predicted at nearly arbitrary composition (within some range) and formed by incorporating a certain density of APBs. This produces sloping regions in the voltage profile that correspond to sequences of ordered structures rather than solid solutions. Similar ordering phenomena may very well occur in other systems that stabilize the P3 structure. The occurrence of such orderings may also give rise to more exotic diffusion mechanisms than are usually considered. For example, diffusion could occur exclusively along 'diluted' APBs [43], resulting in reduced dimensionality of transport, or by creation/annihilation of APBs in waves throughout the crystal. Detailed kinetic studies are required to resolve these mechanisms exactly.

7. Stacking sequence changes

Stacking sequence changes in layered intercalation compounds can be accomplished by a simple shearing of the MX_2 slabs. These transitions tend to be more prevalent in intercalation compounds containing larger ions such as Na and K since they can stabilize prismatic coordination. O3 typically transitions to P3 towards the beginning of charge (deintercalation), while empty layers take on O1 stacking towards the end of charge to form hybrid structures (consisting of a mix of O1 and O3 or O1 and P3 layers) and eventually purely O1. These stacking sequence changes are accompanied by a collective reordering of the intercalant within the layers as the composition changes. Such transitions are critical to battery performance and can lead to mechanical degradation of electrode materials.

Despite the prevalence and importance of stacking sequence changes, the finer details of these processes are not well understood. First-principles techniques can be used to gain some insights into these transitions that may be difficult to probe experimentally. A fundamental property of interest here is the generalized stacking fault energy or γ-surface, which gives the energy per unit area of shearing half of a crystal relative to the other half [75,76]. This has long been recognized as a key property that influences deformation behaviour in metallic alloys [77–80]. The stable points corresponding to local minima of the γ-surface represent allowed stackings, while the unstable points, which are experimentally inaccessible, give the barriers between those stackings. This information provides a starting point for understanding stacking sequence changes as well as key parameters for multiscale modelling efforts.

Figure 8 illustrates the methodology of our γ-surface calculations. Supercells with three MX_2 slabs are used to isolate faults from their periodic images. A displacement $\mathbf{u}$ within the $\mathbf{a}$–$\mathbf{b}$ plane is introduced by adjusting the $\mathbf{c}$ lattice vector ($\mathbf{c}' = \mathbf{c} + \mathbf{u}$), which changes the stacking between each periodic supercell and the next. For each displacement $\mathbf{u}$, we optimize the interlayer

Downloaded from https://royalsocietypublishing.org/ on 24 February 2025

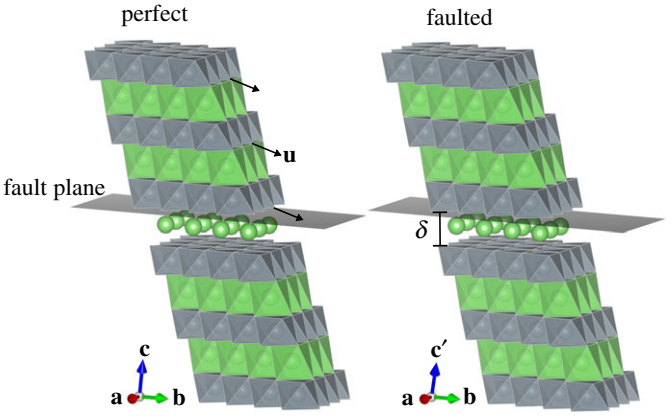

Figure 8. Stacking of an O3 AMX_2 supercell before and after shearing by $\mathrm{u} = (\mathrm{a}/2) + (\mathrm{b}/2)$. The displacement vector u has been scaled up by a factor of three for better visibility. *M* and *A* ions are shown as grey and green, respectively, with *X* anions at the corners of all octahedra. The fault plane is shown in grey. Structure visualization created using VESTA [44]. (Online version in colour.)

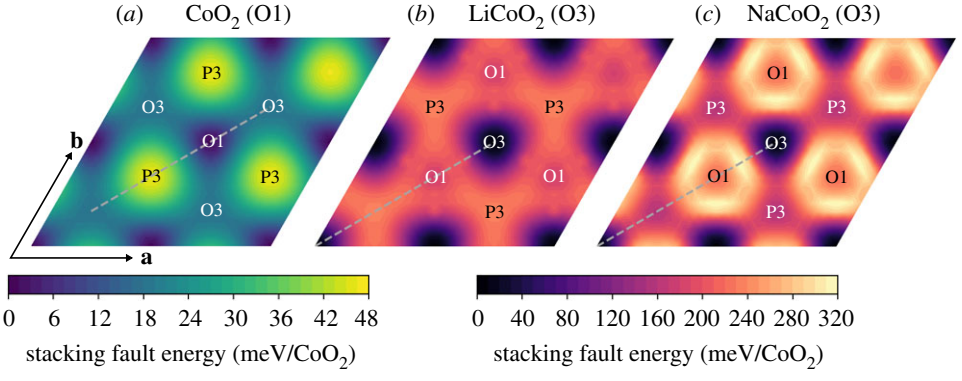

Figure 9. Calculated γ-surfaces of (*a*) O1 CoO_2, (*b*) O3 $LiCoO_2$ and (*c*) O3 $NaCoO_2$, normalized by the number of in-plane formula units. Special points on the surface are annotated with the local stacking. (Online version in colour.)

spacing δ around the fault plane as well as the position of the intercalant ion nearest to the fault plane. More details about the calculations are described in the Methods section. Figure 9 shows calculated γ-surfaces of CoO_2 in the O1 structure and $LiCoO_2$ and $NaCoO_2$ in the O3 structure. Each point on these surfaces corresponds to a particular displacement vector **u**, with the colour representing the stacking fault energy (normalized by the number of in-plane formula units). Special points are labelled with the *local stacking* of the oxygen layers around the fault plane (O1, O3 or P3) although the remaining layers retain their original stacking, as illustrated in figure 8. Note the difference in energy scales between the three compositions: the highest point for $LiCoO_2$ is about five times that of CoO_2, while the highest point for $NaCoO_2$ is about 30% higher than that of $LiCoO_2$. The energy landscape is relatively flat in CoO_2 because the interlayer interactions are mainly limited to van der Waals forces. The presence of an intercalant raises the energy through *A*–O and *A*–Co interactions, which are more significant with the larger and more electropositive Na than Li. Another important detail is the threefold symmetry of the crystal, which is reflected in the γ-surfaces. With this underlying symmetry, there are three equivalent directions for a given stacking sequence transition to occur, so it may not proceed in the same crystallographic direction

Downloaded from https://royalsocietypublishing.org/ on 24 February 2025

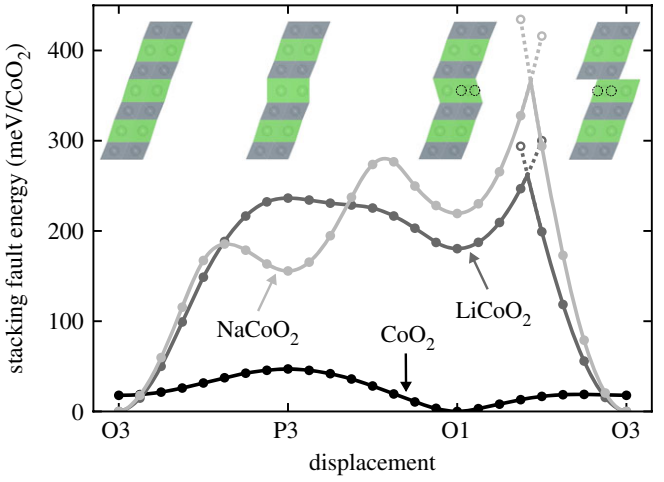

Figure 10. Stacking fault energy along the [110] direction (grey dashed lines in figure 9) for CoO_2, $LiCoO_2$ and $NaCoO_2$, normalized by the number of in-plane formula units. Circles indicate calculated points. Filled circles and solid lines represent equilibrium fault energies, while open circles and dotted lines represent metastable fault energies. Inset supercells show the most stable local *A* coordination within the O3 structure for $LiCoO_2$ and $NaCoO_2$ at each special point on the γ-surface. Black dotted circles in the insets identify vacant tetrahedral *A* sites within the structures. Structure visualization created using VESTA [44]. (Online version in colour.)

going forward and backward even if it is completely reversible. This entropic effect can lead to 'electrochemical creep' after many cycles, resulting in roughening of the electrode particles [14].

To compare the γ-surfaces from figure 9 more closely, we examine the energy along the dotted line connecting O3 to P3 to O1 to O3, shown in figure 10. The preferred coordination of the intercalant in the fault plane at each special point is also shown. For both $LiCoO_2$ and $NaCoO_2$, the intercalant favours prismatic coordination in a local P3 stacking and octahedral (as opposed to tetrahedral) coordination in a local O1 stacking. However, the relative stabilities of each local stacking are different. In $NaCoO_2$, local P3 stacking is more favourable than O1, and both are local minima. In $LiCoO_2$, the situation is reversed, and P3 is actually an unstable maximum. This confirms the established fact that Li is too small to stabilize prismatic coordination. The CoO_2 curve has its lowest value in O1, has a local minimum in a local O3 stacking, and has a maximum for a local P3 stacking, with smooth transitions in between. By contrast, the curves for $LiCoO_2$ and $NaCoO_2$ are mostly smooth but both contain a sharp cusp between the O1 and O3 minima that corresponds to an abrupt change in the intercalant position as the structure is sheared. The smooth transitions (O3 $\leftrightarrow$ P3 and P3 $\leftrightarrow$ O1) require the intercalant to travel along with either the top or bottom layer as the crystal is sheared. However, for the O1 $\leftrightarrow$ O3 transition, if the intercalant travels continuously along with either the top or bottom layer it moves toward a tetrahedral site (black dotted circles in the insets of figure 10), which is higher in energy than the preferred octahedral site. The presence of this cusp feature highlights an important subtlety of γ-surfaces in layered intercalation compounds in that careful consideration of intercalant site preference must be accounted for when calculating them.

The γ-surfaces of figure 9 collect the energies associated with a homogeneous shear of adjacent MX_2 slabs in layered intercalation compounds. However, these materials do not undergo stacking sequence changes via the macroscopic collective shearing of an entire particle. Much like in metallic alloys, the transitions are instead likely mediated by dislocation motion, which requires less energy [76,81,82]. Dislocations have also been observed in intercalation compounds [45,82–88]. The details of their behaviour, however, are still largely a mystery, so we will simply present some underlying concepts.

Downloaded from https://royalsocietypublishing.org/ on 24 February 2025

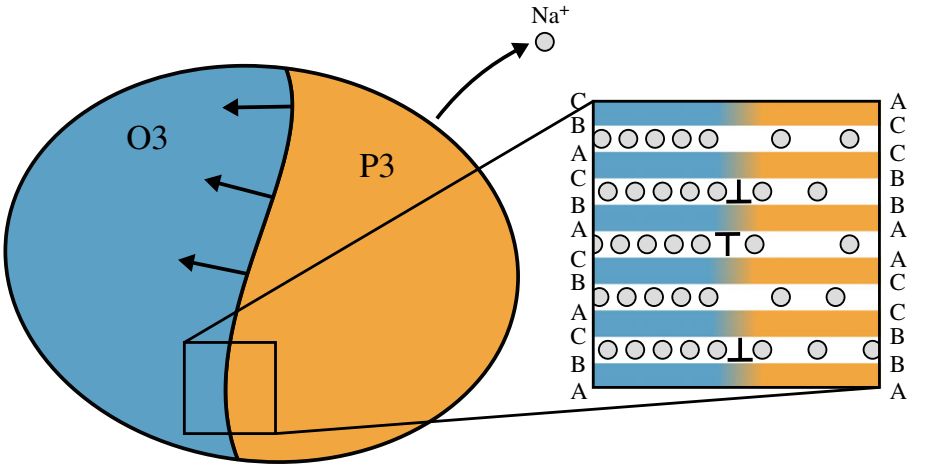

Figure 11. Depiction of an electrode particle undergoing a first-order transition from O3 to P3 upon deintercalation of Na. Inset shows a suggested dislocation structure at the interface. (Online version in colour.)

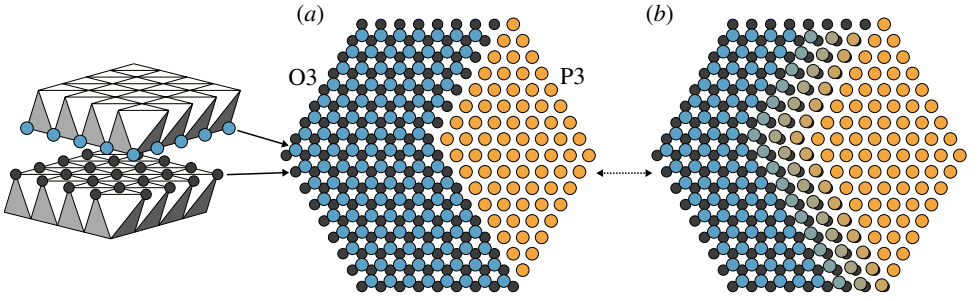

Figure 12. Dislocation structure of an O3/P3 two-phase region viewed along the stacking direction, showing only the two *X* anion layers nearest to the fault plane. The layer below is shown in dark grey, while the layer above is shown in blue or orange for O3 or P3, respectively. In (*a*), the change in stacking is abrupt, while in (*b*), it is more continuous, as reflected by the colour gradient. (Online version in colour.)

Figure 11 schematically illustrates an electrode particle as it transitions from O3 to P3 upon deintercalation of Na. During the transition, the two phases coexist within the same particle and are separated by a moving front at which a stacking sequence change from O3 to P3 must occur. These local changes in the stacking sequence are likely to be mediated by a periodic array of dislocations as schematically represented by right side up and upside down 'T' symbols. By simply considering the *X* anion stacking sequences of the two structures (AB CA BC for O3 versus AB BC CA for P3), we arrive at the dislocation structure shown in the inset of figure 11. Because O3 and P3 have the same stacking periodicity, every third layer is continuous, while pairs of dislocations must be introduced along the phase boundary to accommodate the change in stacking. Another important detail is the depletion of Na locally within the P3 phase. A severe gradient in composition may result in a large interlayer spacing mismatch along the boundary and lead to cracking.

In figure 12, we show what the dislocation structure along the phase front may look like within the *X* layers. The *X* layer below the intercalant layer is shown in dark grey, while the layer above is shown in blue or orange, depending on the stacking. Dislocation lines may change directions or form kinks throughout the particle. The dislocation structure may also consist of a sudden change

Downloaded from https://royalsocietypublishing.org/ on 24 February 2025

between the two stackings or a more continuous transition. The former would result in large local strain of the layers but a lower stacking fault energy (figure 12*a*), while the latter would result in smaller strain and higher stacking fault energy (figure 12*b*). The competition between strain and stacking fault energies should, therefore, determine how spread out the dislocation is. A clearer picture of these dislocations and their motion will provide a better understanding of stacking sequence changes and perhaps how to mitigate them.

8. Conclusion

As battery research pushes beyond Li-ion technology into less well-explored territory, a fundamental understanding of materials in these composition spaces must be developed. We have illustrated the utility of first-principles techniques to predict detailed behaviour of electrode materials. In both layered and spinel host structures, simple size and electrostatic effects can explain thermodynamic trends with varying host and intercalant identities. These include site preferences in spinel, as well as the relative stability of various layered phases and intercalant orderings.

We have highlighted two phenomena that are more prevalent in layered Na intercalation compounds than their Li counterparts: complex Na-vacancy orderings and phase transitions involving shearing of the host layers. Staircases of ordered superstructures that incorporate composition changes through APBs likely have profound implications for Na diffusion, while stacking sequence changes can cause increased susceptibility to mechanical degradation.

Our examination of stacking sequence changes suggests potential strategies that could be developed to avoid them. These transitions may be prevented or delayed thermodynamically through tuning of the host chemistry and ionicity [89], or kinetically penalized by achieving a high dislocation energy. If they cannot be avoided, then they could perhaps be managed so that they are not as harmful, for instance, by matching lattice parameters of the two endpoint phases [10]. The challenges inherent to intercalating Na and other less traditional cations can hopefully be overcome through a combination of experimental efforts and computational insights in order to develop next-generation electrode materials.

9. Methods

DOS and γ-surface calculations were performed using the Vienna *Ab initio* Simulation Package (VASP) [90–93]. Projector augmented-wave (PAW) method [94,95] pseudopotentials (O, S, Ti_sv, Co, Li and Na_pv) were used, and the optB86b-vdW exchange-correlation functional [96] was selected to accurately capture van der Waals interactions. All calculations were spin-polarized. The DOS calculations employed a plane-wave energy cut-off of 550 eV and a k-point mesh of density 45 Å or higher along each reciprocal lattice vector. These calculations were static and used the linear tetrahedron method [97].

The γ-surface calculations were set up using MULTISHIFTER, a CASM-powered [23] utility for calculating γ-surfaces and universal binding energy curves for arbitrary slip planes in crystals. The code is under active development and is available on GitHub [98]. Supercells for the γ-surface calculations contained three layers with an in-plane size of one formula unit. This was found to be sufficient for isolating faults from their periodic images and converging stacking fault energies to within 2%. The γ-surfaces were calculated using 12 by 12 triangular grids of displacements over the unit cell. Only symmetrically distinct displacements on this grid were calculated. For the energy paths along the [110] direction shown in figure 10, the number of samples was doubled. For each displacement, we varied the interlayer spacing around the fault plane from −0.1 Å to 0.4 Å in increments of 0.1 Å, relative to the original spacing. All ions were kept static, except for the one A ion in the fault plane (for $LiCoO_2$ and $NaCoO_2$), which relaxed until forces converged to within 0.2 eV $Å^{-1}$. To avoid local minimum trapping, we ran three separate calculations for each displacement and interlayer spacing in which we initialized the A ion from each of

Downloaded from https://royalsocietypublishing.org/ on 24 February 2025

the three distinct triangular sublattices. The final energy versus interlayer spacing was fit to a parabola to determine the lowest energy for each displacement and initial A position (in some cases, the fit yielded an R^2 value of less than 0.95 so we simply took the lowest value over the interlayer spacings), and the minimum of these was taken to be the stacking fault energy for each displacement. The γ-surface calculations used a plane-wave energy cut-off of 700 eV and a k-point mesh of density 38 Å along each reciprocal lattice vector. Gaussian smearing of width 0.1 eV was used for the $LiCoO_2$ and $NaCoO_2$ relaxations, while static calculations using the linear tetrahedron method [97] were performed for CoO_2.

Data accessibility. This article has no additional data.

Competing interests. We declare we have no competing interests.

Funding. J.L.K. acknowledges support from the U.S. Department of Energy through the Computational Science Graduate Fellowship (DOE CSGF) under Grant No. DE-FG02-97ER25308. This material is also based upon work supported as part of the NorthEast Center for Chemical Energy Storage (NECCES), an Energy Frontier Research Center funded by the U.S. Department of Energy, Office of Science, Office of Basic Energy Sciences under Award No. DE-SC0012583. We acknowledge support from the Center for Scientific Computing from the CNSI, MRL: an NSF MRSEC (DMR-1720256). Computing resources were also provided by the National Energy Research Scientific Computing Center (NERSC), a U.S. Department of Energy Office of Science User Facility operated under Contract No. DE-AC02-05CH11231.

References

1. Goodenough JB, Park KS. 2013 The Li-Ion rechargeable battery: a perspective. *J. Am. Chem. Soc.* **135**, 1167–1176. (doi:10.1021/ja3091438)
2. Nitta N, Wu F, Lee JT, Yushin G. 2015 Li-Ion battery materials: present and future. *Mater. Today* **18**, 252–264. (doi:10.1016/j.mattod.2014.10.040)
3. Delmas C. 2018 Sodium and sodium-ion batteries: 50 years of research. *Adv. Energy Mater.* **8**, 1703137. (doi:10.1002/aenm.v8.17)
4. Hwang JY, Myung ST, Sun YK. 2018 Recent progress in rechargeable potassium batteries. *Adv. Funct. Mater.* **28**, 1802938. (doi:10.1002/adfm.v28.43)
5. Yoo HD, Shterenberg I, Gofer Y, Gershinsky G, Pour N, Aurbach D. 2013 Mg rechargeable batteries: an on-going challenge. *Energy Environ. Sci.* **6**, 2265–2279. (doi:10.1039/c3ee40871j)
6. Ponrouch A, Frontera C, Bardé F, Palacín MR. 2016 Towards a calcium-based rechargeable battery. *Nat. Mater.* **15**, 169–172. (doi:10.1038/nmat4462)
7. Mizushima K, Jones PC, Wiseman PJ, Goodenough JB. 1980 Li_xCoO_2 ($0 < x \leq 1$): a new cathode material for batteries of high energy density. *Mater. Res. Bull.* **15**, 783–789. (doi:10.1016/0025-5408(80)90012-4)
8. Radin MD *et al.* 2017 Narrowing the gap between theoretical and practical capacities in Li-ion layered oxide cathode materials. *Adv. Energy Mater.* **7**, 1602888. (doi:10.1002/aenm.201602888)
9. Han MH, Gonzalo E, Singh G, Rojo T. 2015 A comprehensive review of sodium layered oxides: powerful cathodes for Na-ion batteries. *Energy Environ. Sci.* **8**, 81–102. (doi:10.1039/C4EE03192J)
10. Mariyappan S, Wang Q, Tarascon JM. 2018 Will sodium layered oxides ever be competitive for sodium ion battery applications? *J. Electrochem. Soc.* **165**, A3714–A3722. (doi:10.1149/2.0201816jes)
11. Berthelot R, Carlier D, Delmas C. 2011 Electrochemical investigation of the P2–Na_xCoO_2 phase diagram. *Nat. Mater.* **10**, 74–80. (doi:10.1038/nmat2920)
12. Kubota K, Ikeuchi I, Nakayama T, Takei C, Yabuuchi N, Shiiba H, Nakayama M, Komaba S. 2015 New insight into structural evolution in layered $NaCrO_2$ during electrochemical sodium extraction. *J. Phys. Chem. C* **119**, 166–175. (doi:10.1021/jp5105888)
13. Didier C, Guignard M, Suchomel MR, Carlier D, Darriet J, Delmas C. 2016 Thermally and electrochemically driven topotactical transformations in sodium layered oxides Na_xVO_2. *Chem. Mater.* **28**, 1462–1471. (doi:10.1021/acs.chemmater.5b04882)
14. Radin MD, Alvarado J, Meng YS, Van der Ven A. 2017 Role of crystal symmetry in the reversibility of stacking-sequence changes in layered intercalation electrodes. *Nano Lett.* **17**, 7789–7795. (doi:10.1021/acs.nanolett.7b03989)

Downloaded from https://royalsocietypublishing.org/ on 24 February 2025

15. Li X *et al.* 2014 Direct visualization of the Jahn-Teller effect coupled to Na ordering in $Na_{5/8}MnO_2$. *Nat. Mater.* **13**, 586–592. (doi:10.1038/nmat3964)
16. Vassilaras P, Kwon DH, Dacek ST, Shi T, Seo DH, Ceder G, Kim JC. 2017 Electrochemical properties and structural evolution of O3-type layered sodium mixed transition metal oxides with trivalent nickel. *J. Mater. Chem. A* **5**, 4596–4606. (doi:10.1039/C6TA09220A)
17. Clément RJ, Bruce PG, Grey CP. 2015 Review—manganese-based P2-type transition metal oxides as sodium-ion battery cathode materials. *J. Electrochem. Soc.* **162**, A2589–A2604. (doi:10.1149/2.0201514jes)
18. Willis TJ, Porter DG, Voneshen DJ, Uthayakumar S, Demmel F, Gutmann MJ, Roger M, Refson K, Goff JP. 2018 Diffusion mechanism in the sodium-ion battery material sodium cobaltate. *Sci. Rep.* **8**, 3210. (doi:10.1038/s41598-018-21354-5)
19. Liu M, Rong Z, Malik R, Canepa P, Jain A, Ceder G, Persson KA. 2015 Spinel compounds as multivalent battery cathodes: a systematic evaluation based on *ab initio* calculations. *Energy Environ. Sci.* **8**, 964–974. (doi:10.1039/C4EE03389B)
20. Kim JR, Amatucci GG. 2015 Structural and electrochemical investigation of Na^+ insertion into high-voltage spinel electrodes. *Chem. Mater.* **27**, 2546–2556. (doi:10.1021/acs.chemmater.5b00283)
21. Sun X, Bonnick P, Duffort V, Liu M, Rong Z, Persson KA, Ceder G, Nazar LF. 2016 A high capacity thiospinel cathode for Mg batteries. *Energy Environ. Sci.* **9**, 2273–2277. (doi:10.1039/C6EE00724D)
22. Kolli SK, Van der Ven A. 2018 Controlling the electrochemical properties of spinel intercalation compounds. *ACS Appl. Energy Mater.* **1**, 6833–6839. (doi:10.1021/acsaem.8b01080)
23. CASM Developers. CASM v0.3.X.; 2019: Available from: https://github.com/prisms-center/CASMcode.
24. Thomas JC, Van der Ven A. 2013 Finite-temperature properties of strongly anharmonic and mechanically unstable crystal phases from first principles. *Phys. Rev. B* **88**, 214111. (doi:10.1103/PhysRevB.88.214111)
25. Van der Ven A, Thomas JC, Puchala B, Natarajan AR. 2018 First-principles statistical mechanics of multicomponent crystals. *Annu. Rev. Mater. Res.* **48**, 27–55. (doi:10.1146/annurev-matsci-070317-124443)
26. Puchala B, Van der Ven A. 2013 Thermodynamics of the Zr–O system from first-principles calculations. *Phys. Rev. B* **88**, 094108. (doi:10.1103/PhysRevB.88.094108)
27. Van der Ven A, Ceder G, Asta M, Tepesch PD. 2001 First-principles theory of ionic diffusion with nondilute carriers. *Phys. Rev. B* **64**, 184307. (doi:10.1103/PhysRevB.64.184307)
28. Van der Ven A, Thomas JC, Xu Q, Swoboda B, Morgan D. 2008 Nondilute diffusion from first principles: Li diffusion in Li_xTiS_2. *Phys. Rev. B* **78**, 104306. (doi:10.1103/PhysRevB.78.104306)
29. Bhattacharya J, Van der Ven A. 2011 First-principles study of competing mechanisms of nondilute Li diffusion in spinel Li_xTiS_2. *Phys. Rev. B* **83**, 144302. (doi:10.1103/PhysRevB.83.144302)
30. Van der Ven A, Bhattacharya J, Belak AA. 2013 Understanding Li diffusion in Li-intercalation compounds. *Acc. Chem. Res.* **46**, 1216–1225. (doi:10.1021/ar200329r)
31. Islam MS, Fisher CAJ. 2014 Lithium and sodium battery cathode materials: computational insights into voltage, diffusion and nanostructural properties. *Chem. Soc. Rev.* **43**, 185–204. (doi:10.1039/C3CS60199D)
32. Levi E, Gofer Y, Aurbach D. 2010 On the way to rechargeable Mg batteries: the challenge of new cathode materials. *Chem. Mater.* **22**, 860–868. (doi:10.1021/cm9016497)
33. Yabuuchi N, Kubota K, Dahbi M, Komaba S. 2014 Research development on sodium-ion batteries. *Chem. Rev.* **114**, 11636–11682. (doi:10.1021/cr500192f)
34. Luntz A. 2015 Beyond lithium ion batteries. *J. Phys. Chem. Lett.* **6**, 300–301. (doi:10.1021/jz502665r)
35. Massé RC, Uchaker E, Cao G. 2015 Beyond Li-ion: electrode materials for sodium- and magnesium-ion batteries. *Sci. China Mater.* **58**, 715–766. (doi:10.1007/s40843-015-0084-8)
36. Kundu D, Talaie E, Duffort V, Nazar LF. 2015 The emerging chemistry of sodium ion batteries for electrochemical energy storage. *Angew. Chem. Int. Ed.* **54**, 3431–3448. (doi:10.1002/anie.201410376)
37. Sapunkov O, Pande V, Khetan A, Choomwattana C, Viswanathan V. 2015 Quantifying the promise of 'beyond' Li-ion batteries. *Transl. Mater. Res.* **2**, 045002. (doi:10.1088/2053-1613/2/4/045002)

Downloaded from https://royalsocietypublishing.org/ on 24 February 2025

38. Choi JW, Aurbach D. 2016 Promise and reality of post-lithium-ion batteries with high energy densities. *Nat. Rev. Mater.* **1**, 16013. (doi:10.1038/natrevmats.2016.13)
39. Kubota K, Dahbi M, Hosaka T, Kumakura S, Komaba S. 2018 Towards K-Ion and Na-Ion batteries as 'Beyond Li-Ion'. *Chem. Rec.* **18**, 459–479. (doi:10.1002/tcr.v18.4)
40. Skundin AM, Kulova TL, Yaroslavtsev AB. 2018 Sodium-ion batteries (a review). *Russ. J. Electrochem.* **54**, 113–152. (doi:10.1134/S1023193518020076)
41. Kohn W, Sham LJ. 1965 Self-consistent equations including exchange and correlation effects. *Phys. Rev.* **140**, A1133–A1138. (doi:10.1103/PhysRev.140.A1133)
42. Sanchez JM, Ducastelle F, Gratias D. 1984 Generalized cluster description of multicomponent systems. *Phys. A: Stat. Mech. Appl.* **128**, 334–350. (doi:10.1016/0378-4371(84)90096-7)
43. Vinckevičiūtė J, Radin MD, Van der Ven A. 2016 Stacking-sequence changes and Na ordering in layered intercalation materials. *Chem. Mater.* **28**, 8640–8650. (doi:10.1021/acs.chemmater.6b03609)
44. Momma K, Izumi F. 2011 VESTA 3 for three-dimensional visualization of crystal, volumetric and morphology data. *J. Appl. Crystallogr.* **44**, 1272–1276. (doi:10.1107/S0021889811038970)
45. Cherns D, Ngo GP. 1983 Electron microscope studies of sodium and lithium intercalation in TiS_2. *J. Solid State Chem.* **50**, 7–19. (doi:10.1016/0022-4596(83)90228-1)
46. Van der Ven A, Aydinol M, Ceder G, Kresse G, Hafner J. 1998 First-principles investigation of phase stability in Li_xCoO_2. *Phys. Rev. B* **58**, 2975. (doi:10.1103/PhysRevB.58.2975)
47. Reed J, Ceder G. 2004 Role of electronic structure in the susceptibility of metastable transition-metal oxide structures to transformation. *Chem. Rev.* **104**, 4513–4533. (doi:10.1021/cr020733x)
48. Kim S, Ma X, Ong SP, Ceder G. 2012 A comparison of destabilization mechanisms of the layered Na_xMO_2 and Li_xMO_2 compounds upon alkali de-intercalation. *Phys. Chem. Chem. Phys.* **14**, 15 571–15 578. (doi:10.1039/c2cp43377j)
49. Delmas C, Braconnier JJ, Fouassier C, Hagenmuller P. 1981 Electrochemical intercalation of sodium in Na_xCoO_2 bronzes. *Solid State Ionics* **3-4**, 165–169. (doi:10.1016/0167-2738(81)90076-X)
50. Kubota K, Yabuuchi N, Yoshida H, Dahbi M, Komaba S. 2014 Layered oxides as positive electrode materials for Na-ion batteries. *MRS Bull.* **39**, 416–422. (doi:10.1557/mrs.2014.85)
51. Wang PF, You Y, Yin YX, Wang YS, Wan LJ, Gu L, Guo Y-G. 2016 Suppressing the P2–O2 phase transition of $Na_{0.67}Mn_{0.67}Ni_{0.33}O_2$ by magnesium substitution for improved sodium-ion batteries. *Angew. Chem. Int. Ed.* **55**, 7445–7449. (doi:10.1002/anie.201602202)
52. Wang Y, Ding Y, Ni J. 2009 Ground-state phase diagram of Na_xCoO_2: correlation of Na ordering with CoO_2 stacking sequences. *J. Phys.: Condens. Matter* **21**, 035401. (doi:10.1088/0953-8984/21/3/035401)
53. Lei Y, Li X, Liu L, Ceder G. 2014 Synthesis and stoichiometry of different layered sodium cobalt oxides. *Chem. Mater.* **26**, 5288–5296. (doi:10.1021/cm5021788)
54. Shannon RD. 1976 Revised effective ionic radii and systematic studies of interatomic distances in halides and chalcogenides. *Acta Crystallogr. Sect. A* **32**, 751–767. (doi:10.1107/S0567739476001551)
55. Dresselhaus MS, Dresselhaus G, Jorio A. 2007 *Group theory: application to the physics of condensed matter*. Berlin (Heidelberg/New York): Springer.
56. Pavarini E, Koch E, Anders F, Jarrell M (eds). 2012 *Correlated electrons: from models to materials. Modeling and simulation*, vol. 2. Verlag des Forschungszentrum Jülich.
57. Radin MD, Van der Ven A. 2016 Stability of prismatic and octahedral coordination in layered oxides and sulfides intercalated with alkali and alkaline-earth metals. *Chem. Mater.* **28**, 7898–7904. (doi:10.1021/acs.chemmater.6b03454)
58. Croguennec L, Pouillerie C, Mansour AN, Delmas C. 2001 Structural characterisation of the highly deintercalated $Li_xNi_{1.02}O_2$ phases (with $x \leq 0.30$). *J. Mater. Chem.* **11**, 131–141. (doi:10.1039/b003377o)
59. Emly A, Van der Ven A. 2015 Mg intercalation in layered and spinel host crystal structures for Mg batteries. *Inorg. Chem.* **54**, 4394–4402. (doi:10.1021/acs.inorgchem.5b00188)
60. Kolli SK, Van der Ven A. 2018 First-principles study of spinel $MgTiS_2$ as a cathode material. *Chem. Mater.* **30**, 2436–2442. (doi:10.1021/acs.chemmater.8b00552)
61. Kaufman JL, Van der Ven A. 2019 Na_xCoO_2 phase stability and hierarchical orderings in the O3/P3 structure family. *Phys. Rev. Mater.* **3**, 015402. (doi:10.1103/PhysRevMaterials.3.015402)

Downloaded from https://royalsocietypublishing.org/ on 24 February 2025

62. Thompson AH. 1979 Electrochemical potential spectroscopy: a new electrochemical measurement. *J. Electrochem. Soc.* **126**, 608–616. (doi:10.1149/1.2129095)
63. Winn DA, Shemilt JM, Steele BCH. 1976 Titanium disulphide: a solid solution electrode for sodium and lithium. *Mater. Res. Bull.* **11**, 559–566. (doi:10.1016/0025-5408(76)90239-7)
64. Kubota K, Asari T, Yoshida H, Yaabuuchi N, Shiiba H, Nakayama M, Komaba S. 2016 Understanding the structural evolution and redox mechanism of a $NaFeO_2$-$NaCoO_2$ solid solution for sodium-ion batteries. *Adv. Funct. Mater.* **26**, 6047–6059. (doi:10.1002/adfm.v26.33)
65. Bonnick P, Sun X, Lau KC, Liao C, Nazar LF. 2017 Monovalent versus divalent cation diffusion in thiospinel Ti_2S_4. *J. Phys. Chem. Lett.* **8**, 2253–2257. (doi:10.1021/acs.jpclett.7b00618)
66. Aykol M, Kim S, Wolverton C. 2015 Van der Waals interactions in layered lithium cobalt oxides. *J. Phys. Chem. C* **119**, 19 053–19 058. (doi:10.1021/acs.jpcc.5b06240)
67. Hironaka Y, Kubota K, Komaba S. 2017 P2- and P3-K_xCoO_2 as an electrochemical potassium intercalation host. *Chem. Commun.* **53**, 3693–3696. (doi:10.1039/C7CC00806F)
68. Hwang JY, Kim J, Yu TY, Myung ST, Sun YK. 2018 Development of P3-$K_{0.69}CrO_2$ as an ultra-high-performance cathode material for K-ion batteries. *Energy Environ. Sci.* **11**, 2821–2827. (doi:10.1039/C8EE01365A)
69. Toriyama MY, Kaufman JL, Van der Ven A. 2019 Potassium ordering and structural phase stability in layered K_xCoO_2. *ACS Appl. Energy Mater.* **2**, 2629–2636. (doi:10.1021/acsaem.8b02238)
70. Maazaz A, Delmas C, Hagenmuller P. 1983 A study of the Na_xTiO_2 system by electrochemical deintercalation. *J. Inclusion Phenom.* **1**, 45–51. (doi:10.1007/BF00658014)
71. Wu D, Li X, Xu B, Twu N, Liu L, Ceder G. 2015 $NaTiO_2$: a layered anode material for sodium-ion batteries. *Energy Environ. Sci.* **8**, 195–202. (doi:10.1039/C4EE03045A)
72. Huang Q, Foo ML, Lynn JW, Zandbergen HW, Lawes G, Wang Y *et al.* 2004 Low temperature phase transitions and crystal structure of $Na_{0.5}CoO_2$. *J. Phys.: Condens. Matter* **16**, 5803–5814. (doi:10.1088/0953-8984/16/32/016)
73. Guignard M, Didier C, Darriet J, Bordet P, Elkaïm E, Delmas C. 2013 P2-Na_xVO_2 system as electrodes for batteries and electron-correlated materials. *Nat. Mater.* **12**, 74–80. (doi:10.1038/nmat3478)
74. Yabuuchi N, Ikeuchi I, Kubota K, Komaba S. 2016 Thermal stability of Na_xCrO_2 for rechargeable sodium batteries; studies by high-temperature synchrotron X-ray diffraction. *ACS Appl. Mater. Interfaces* **8**, 32 292–32 299. (doi:10.1021/acsami.6b09280)
75. Vítek V. 1968 Intrinsic stacking faults in body-centred cubic crystals. *Phil. Mag.* **18**, 773–786. (doi:10.1080/14786436808227500)
76. Christian JW, Vítek V. 1970 Dislocations and stacking faults. *Rep. Prog. Phys.* **33**, 307–411. (doi:10.1088/0034-4885/33/1/307)
77. Yamaguchi M, Umakoshi Y. 1990 The deformation behaviour of intermetallic superlattice compounds. *Prog. Mater. Sci.* **34**, 1–148. (doi:10.1016/0079-6425(90)90002-Q)
78. Lu G, Kioussis N, Bulatov VV, Kaxiras E. 2000 Generalized-stacking-fault energy surface and dislocation properties of aluminum. *Phys. Rev. B* **62**, 3099–3108. (doi:10.1103/PhysRevB.62.3099)
79. Van Swygenhoven H, Derlet PM, Frøseth AG. 2004 Stacking fault energies and slip in nanocrystalline metals. *Nat. Mater.* **3**, 399–403. (doi:10.1038/nmat1136)
80. Kibey S, Liu JB, Johnson DD, Sehitoglu H. 2007 Predicting twinning stress in FCC metals: linking twin-energy pathways to twin nucleation. *Acta Mater.* **55**, 6843–6851. (doi:10.1016/j.actamat.2007.08.042)
81. Hull D, Bacon DJ. 2001 *Introduction to dislocations*. London, UK: Butterworth-Heinemann.
82. Gabrisch H, Yazami R, Fultz B. 2002 The character of dislocations in $LiCoO_2$. *Electrochem. Solid-State Lett.* **5**, A111–A114. (doi:10.1149/1.1472257)
83. Dresselhaus MS, Dresselhaus G. 1981 Intercalation compounds of graphite. *Adv. Phys.* **30**, 139–326. (doi:10.1080/00018738100101367)
84. Remškar M, Popović A, Starnberg HI. 1999 Stacking transformation and defect creation in Cs intercalated TiS_2 single crystals. *Surface Sci.* **430**, 199–205. (doi:10.1016/S0039-6028(99)00442-2)
85. Ulvestad A, Singer A, Clark JN, Cho HM, Kim JW, Harder R, Maser J, Meng YS, Shpyrko OG. 2015 Topological defect dynamics in operando battery nanoparticles. *Science* **348**, 1344–1347. (doi:10.1126/science.aaa1313)

Downloaded from https://royalsocietypublishing.org/ on 24 February 2025

86. Clément RJ, Middlemiss DS, Seymour ID, Ilott AJ, Grey CP. 2016 Insights into the nature and evolution upon electrochemical cycling of planar defects in the β-$NaMnO_2$ Na-ion battery cathode: an NMR and first-principles density functional theory approach. *Chem. Mater.* **28**, 8228–8239. (doi:10.1021/acs.chemmater.6b03074)
87. Li Q, Yao Z, Wu J, Mitra S, Hao S, Sahu TS, Li Y, Wolverton C, Dravid VP. 2017 Intermediate phases in sodium intercalation into MoS_2 nanosheets and their implications for sodium-ion batteries. *Nano Energy* **38**, 342–349. (doi:10.1016/j.nanoen.2017.05.055)
88. Bai X, *et al.* 2018 Anionic redox activity in a newly Zn-doped sodium layered oxide P2-$Na_{2/3}Mn_{1-y}Zn_yO_2$ ($0 < y < 0.23$). *Adv. Energy Mater.* **8**, 1802379. (doi:10.1002/aenm.v8.32)
89. Sathiya M, Jacquet Q, Doublet ML, Karakulina OM, Hadermann J, Tarascon JM. 2018 A chemical approach to raise cell voltage and suppress phase transition in O3 sodium layered oxide electrodes. *Adv. Energy Mater.* **8**, 1702599. (doi:10.1002/aenm.201702599)
90. Kresse G, Hafner J. 1993 *Ab initio* molecular dynamics for liquid metals. *Phys. Rev. B* **47**, 558. (doi:10.1103/PhysRevB.47.558)
91. Kresse G, Hafner J. 1994 *Ab initio* molecular-dynamics simulation of the liquid-metalamorphous-semiconductor transition in germanium. *Phys. Rev. B* **49**, 14251. (doi:10.1103/PhysRevB.49.14251)
92. Kresse G, Furthmüller J. 1996 Efficiency of *ab initio* total energy calculations for metals and semiconductors using a plane-wave basis set. *Comput. Mater. Sci.* **6**, 15–50. (doi:10.1016/0927-0256(96)00008-0)
93. Kresse G, Furthmüller J. 1996 Efficient iterative schemes for *ab initio* total-energy calculations using a plane-wave basis set. *Phys. Rev. B* **54**, 11169. (doi:10.1103/PhysRevB.54.11169)
94. Blöchl PE. 1994 Projector augmented-wave method. *Phys. Rev. B* **50**, 17953. (doi:10.1103/PhysRevB.50.17953)
95. Kresse G, Joubert D. 1999 From ultrasoft pseudopotentials to the projector augmented-wave method. *Phys. Rev. B* **59**, 1758. (doi:10.1103/PhysRevB.59.1758)
96. Klimeš J, Bowler DR, Michaelides A. 2010 Chemical accuracy for the van der Waals density functional. *J. Phys.: Condens. Matter* **22**, 022201. (doi:10.1088/0953-8984/22/2/022201)
97. Blöchl PE, Jepsen O, Andersen OK. 1994 Improved tetrahedron method for Brillouin-zone integrations. *Phys. Rev. B* **49**, 16223. (doi:10.1103/PhysRevB.49.16223)
98. Goiri JG. multishifter; 2019: Available from: https://github.com/goirijo/multishifter.